Structure and Chemical Composition of Soil C-Rich Al–Si–Fe Coprecipitates at Nanometer Scale

Floriane Jamoteau, Nithavong Cam, Clément Levard, Emmanuel Doelsch, Ghislain Gassier, Adrien Duvivier, Adrien Boulineau, François Saint-Antonin, Isabelle Basile-Doelsch

Structure and chemical composition of soil C-rich Al-Si-Fe-coprecipitates at nanometer scale

Floriane Jamoteau[1,2,3†], Nithavong Cam[1], Clément Levard[1], Emmanuel Doelsch[1,2,3], Ghislain Gassier[1], Adrien Duvivier[1], Adrien Boulineau[4], François Saint-Antonin[4], Isabelle Basile-Doelsch[1]*

[1]Aix Marseille University, CNRS, IRD, INRAE, Coll France, CEREGE, Aix-en-Provence, France ; [2]CIRAD, UPR Recyclage et risque, F-34398 Montpellier, France ; [3]Recyclage et Risque, Univ Montpellier, CIRAD, Montpellier, France ; [4]Université Grenoble Alpes, CEA, LITEN, Grenoble, France.

*Corresponding Author: floriane.jamoteau@unil.ch.

†Present Addresses: Institute of Earth Surface Dynamics, University of Lausanne, Lausanne, Switzerland

ABSTRACT. Soil carbon stabilization is mainly driven by organo-mineral interactions. Coprecipitates, of organic matter with short-range order minerals, detected through indirect chemical extraction methods, are increasingly recognized as key carbon sequestration phases. Yet the atomic structure of these coprecipitates is still rather conceptual. We used transmission electron microscopy imaging combined with EDX (energy dispersive x-ray) and EELS (electron energy loss spectroscopy) chemical mappings, which enabled direct nanoscale characterization of coprecipitates from Andosols. A comparison with reference synthetic coprecipitates showed that the natural coprecipitates were structured by an amorphous Al, Si and Fe inorganic skeleton associated with C, and were therefore even less organized than short-range order minerals usually described. These amorphous type of coprecipitates resembled previously conceptualized nanosized coprecipitates of inorganic oligomers with organics (nanoCLICs) with heterogeneous elemental proportions (of C, Al, Si and Fe) at nanoscale. These results mark a new step in the high-resolution imaging of organo-mineral associations, while shedding further light on the mechanisms that control carbon stabilization in soil, and more broadly in aquatic colloid, sediment and extraterrestrial samples.

KEYWORDS. Soil carbon cycle, organic matter, organo-mineral associations, coprecipitates, transmission electron microscopy, EDX, EELS.

SHORT SYNOPSIS STATEMENT.

Structural characterization of organo-mineral associations of soils remains limited. This study provides chemical mapping down to a few nanometers of the structure of these associations,

leading to a new conceptualization of the latter with implications for their fate and stability in soils.

INTRODUCTION

Soil is the third largest reservoir of organic carbon (C) on Earth[1]. A large part of this organic C is found in form of organic compounds bound to minerals[2–4], thereby shielding them from microbial mineralization[5], which accounts for one of the mechanisms for long-term organic carbon persistence [6,7]. These associations includes two interaction mechanisms at the molecular scale: adsorption and coprecipitation[3,8]. Adsorption refers to accumulation of organic compounds on primary or secondary mineral surface with various bond types (classified as chemisorption or physisorption). As for the formation of co-precipitates in soil, as defined by Kleber et al.[3], it may involve several interacting processes (complexation, precipitation and adsorption) between OM and metal (mainly Fe and Al) species hydrolyzed, insolubilized and/or oxidized. In soils with acidic pH ($\leqslant$~7), organo-mineral associations mainly involve coprecipitates formed by precipitation of organic compounds with secondary mineral phases or with elements derived from mineral weathering containing Fe and Al[9–12]. Coprecipitates are thought to have a major role in soil C sequestration[12], yet their chemical composition and 3D atomic structure using conventional geochemical techniques has been substantially hampered by three main challenges.

The first challenge relates to the analytical methods for detecting coprecipitates in soils. Coprecipitates, in terms of crystalline structure, are intermediate between allophane and metal-organic association. To detect this type of crystalline structure, wet-chemical extraction of soil is a standard procedure (e.g. extracted by Na-pyrophosphate and to some extent by ammonium oxalate–oxalic or hydroxylamine[13,14]). Following these chemical extractions, the ionic

concentrations in solution (e.g. Fe, Al or Si) are used to recalculate the quantities of phases initially present in the soil. Moreover, for some extractions (Na-pyrophosphate and hydroxylamine) the detection of C in solution is used to detect its association with this type of crystalline structure, presumably in the form of coprecipitates. However, no structural information on coprecipitates can be obtained as wet-chemical extractions destroy the phases of interest.

The second challenge concerns lab experiments. As it is hard to extract intact coprecipitates from soils, in many studies they have been characterized using synthetic coprecipitates obtained by coprecipitating organic matter (OM) with two metals, i.e. with Fe[15–25] and sometimes with Al[26–28]. The choice of these metals is linked to their high complexation capacity with OM (Figure 1), and also to the fact that they are major elements in terms of concentration in most soils. However, the assumption that only these two metals are involved in coprecipitate formation in soils is simplistic since many other chemical elements derived from the weathering of soil minerals (e.g. Si, Mg^{2+}, K^{+}, Na or Ca) are also present in the soil solutions in which coprecipitation occurs.

The third challenge relates to the conceptual models used to represent coprecipitates at molecular scales. In the literature, coprecipitates are generally represented by OM in contact with well-known short-range order (SRO) minerals. For Fe, SROs are represented by aggregates of spherical ferrihydrite nanoparticles[3,23], whereas for Al, amorphous Al oxyhydroxide, imogolite or allophane phases are often mentioned but barely represented by a conceptual model, except in Levard et al. (2012)[29] (Figure 1). There are two main reasons for this shortcoming in conceptual molecular scale coprecipitate models: (1) firstly, unlike adsorption models on mineral surfaces[8,30], the surfaces reactivity of the inorganic part of coprecipitates is difficult to determine

and predict, and (2) secondly, carrying out in situ coprecipitate analyses at the nanometric scale with synthetic or natural soil samples is challenging.

Progress on the last two locking points has been achieved in recent laboratory studies. Tamrat et al. (2018, 2019)[31,32] synthesized coprecipitates from a biotite weathering solution. They showed that the mono (K^+) and divalent (Mg^{2+}) ions remained in solution while the coprecipitates formed 5- to -200 nm nanoparticles containing OM, Fe, Al, as well as Si. Using Fe K-edge extended X-ray absorption fine structure (EXAFS) spectroscopy, the local structure of the coprecipitates was modeled as a loose irregular 3D network of amorphous small Fe, Si and Al oligmers forming an amorphous and open-structured inorganic skeleton. Within this inorganic network, the organic compounds would be linked in the network pores by Fe and Al bonds of the skeleton, by monomeric Fe-O-C and Al-O-C, or by weak bonds with another organic molecule (Figure 1). These results gave rise to definition of the nanosized coprecipitates of inorganic oligomers with organics (nanoCLICs) concept. However, direct in situ characterization of nanoCLICs has yet to be achieved.

Substantial advances have also been made in the in situ soil organo-mineral associations analysis field[33]. Transmission electron microscopy (TEM) is the tool of choice to probe coprecipitates at high spatial resolution through the analytical combinations offered by the different sensors available in a single instrument. Electron diffraction can be used to differentiate mineral-crystallized phases from poorly crystallized or even amorphous phases. Energy dispersion X ray (EDX) and electron energy loss (EELS)[34,35] spectroscopy can be used in scanning TEM mode (STEM) to map the nanoscale elemental composition, with elemental colocation resolutions of 10 nm[36,37] and few Å[34,35], respectively. While the spatial resolution of EELS is higher, its sensitivity is not as good as EDX for heavy elements. These two imaging

spectroscopy tools can therefore be used advantageously in a complementary way, but they have yet to be markedly used in soil science research. EDX spectroscopy has mainly been used for spot analyses[38,39,40]. But recently Possinger et al. (2020)[41] took up the challenge of mapping C and N by EELS and revealed soil OM spatial heterogeneity patterns at the 1 nm scale. This latter research has opened a promising avenue for the simultaneous characterization of organic and inorganic coprecipitate phases at the nanoscale.

The aim of this study was to develop a conceptual molecular model of organo-mineral coprecipitates that contribute to soil C stabilization. We focused on an Andosol due the high abundance of these coprecipitates in this type of soil. We analyzed the crystallinity of inorganic phases obtained by electron diffraction and performed STEM-EDX and TEM-EELS imaging to collocate and quantify C, Al, Si and Fe at the nanometric scale. In support of our interpretations of coprecipitate formation in natural systems, we also relied: (1) on synthesized coprecipitates made with inorganic solutions from basalt and labradorite weathering to obtain solutions containing a diverse range of elements closer to the elemental diversity in natural soil solution (these two coprecipitates served as reference coprecitipates, denoted nanoCLICs$_{Basalt}$ and nanoCLICs$_{Labradorite}$) and (2) on statistical approaches based on a Python code we specifically developed for TEM-EELS imaging. Our results demonstrate that the AAndosol coprecipitates are structured by an amorphous Al, Si and Fe inorganic skeleton, and are therefore even less organized than short-range order minerals usually described. These findings provide insights into the nanoscale mechanisms that control C stabilization in soils.

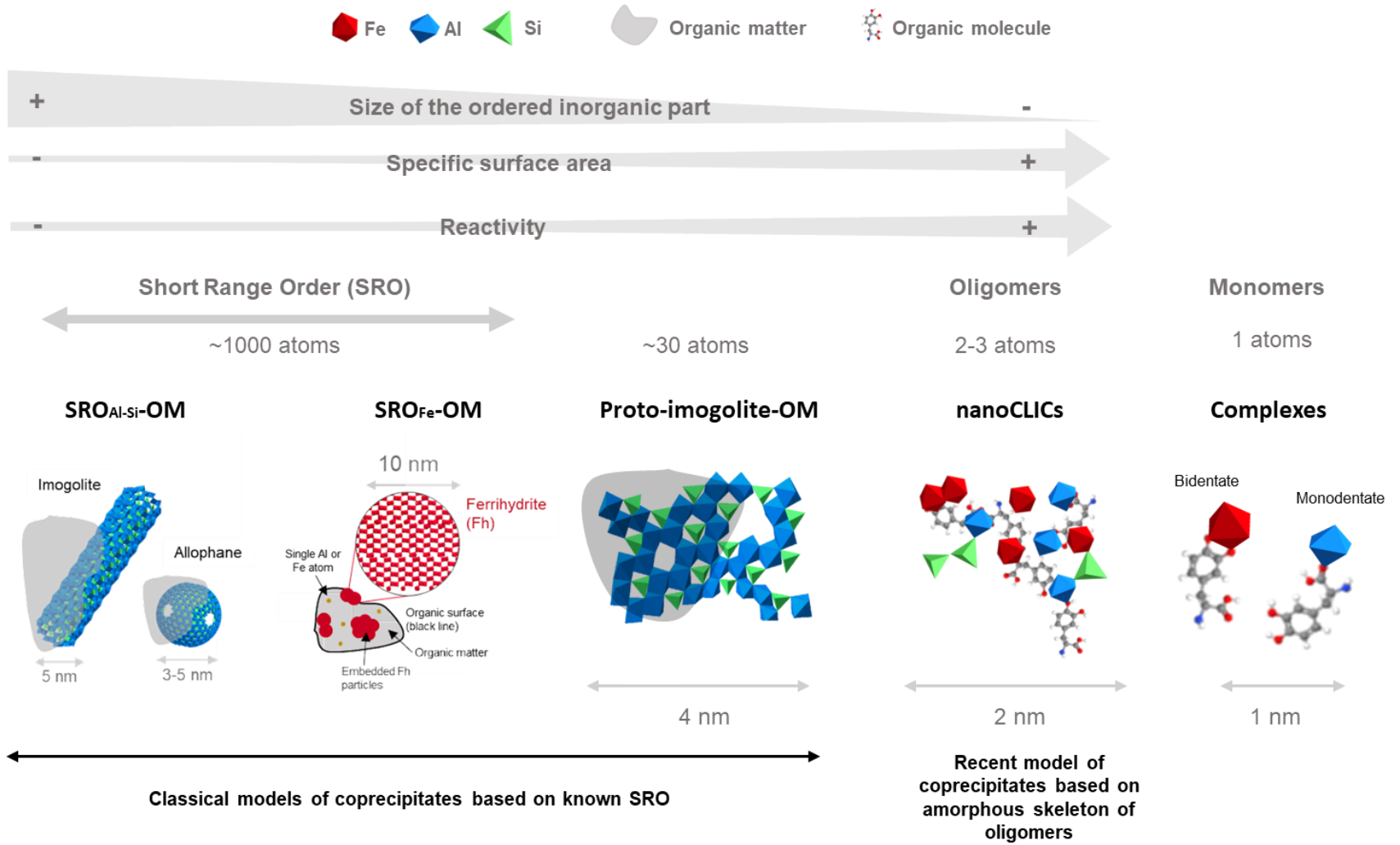

Figure 1. Molecular models of soil coprecipitates in the literature. Coprecipitates can be conceptualized with: (i) an inorganic phase of one or several 100 to 1,000 atoms forming a more or less organized crystal lattice, or so-called short-range orders (SRO). These SRO are imogolites or allophanes (composed of Si and Al) or ferrihydrite (composed of Fe; scheme adapted from Kleber et al.[3]); (ii) an

inorganic phase made up of only ~30 atoms with limited local organization, such as proto-imogolites (scheme adapted from Levard et al.[29]); and (iii) an inorganic phase involving the polymerization of only 2-3 atoms, the inorganic phase is composed of small amorphous oligomers, without local arrangement called nanosized coprecipitates of inorganic oligomers with organics (nanoCLICs) (scheme adapted from Tamrat et al.[32]); and (iv) an inorganic part involving only one atom (e.g. Fe, Al or Ca) complexed with organic molecules through a mono or bidentate bond.

2. MATERIALS AND METHODS

2.1. Synthetic nanoCLICs preparation

Synthetic nanoCLICs were obtained using a protocol similar to that of Tamrat et al. (2019)[32], which consisted of two main steps: (1) silicate weathering to obtain a solution with dissolved elements, and (2) coprecipitation of the dissolved elements with an organic L-3,4-dihydroxyphenylalanine molecule (hereby referred to as DOPA). The DOPA molecule was selected due to its low molecular weight typical of organic compounds and because the DOPA has the main functional groups of MAOM[42]. Moreover, using DOPA also avoided fractionation uncertainty during coprecipitation[32]. This protocol was carried out using two types of minerals or rocks, i.e. basalt and labradorite, to obtain weathered solutions with various dissolved elements.

Briefly, the weathering solutions were obtained as follows: basalt or labradorite were crushed and particles between 50 and 100 µm were isolated by dry sieving. Then, to mimic mineral weathering, 33 g of particles were agitated in 1 L of an HNO_3 solution at 10^{-2}M. After 3 months, the solutions were filtered using tangential flow filtration (KrosFlo®) with a 10 KDa pore size (corresponding to a pore size of about 2 nm). The dissolved elements were measured by ICP-AES (see results in SI1). The weathering solutions were then diluted to obtain an Al+Fe concentration of as low as 1.8 mM according to the protocol of Tamrat et al.[32] (4-fold dilution for the basalt weathering solution and 1.8-fold for the labradorite weathering solution). In a second step, L-3,4-dihydroxyphenylalanine (L-DOPA) was added to 150 ml of the weathering solutions to reach an atomic ratio of (Al+Fe):C = 1 (corresponding to an L-DOPA mass of 5.9 mg). The coprecipitation step involved titration of the solutions with NaOH (0.1 M) at an hydrolysis rate of 600 $\mu L.min^{-1}.L^{-1}$. Titrations were performed at a fixed temperature of 25°C

using a thermostatic bath. Titrations were stopped when the pH reached 5 to be representative of acidic soil conditions (210 min titration time). The coprecipitates obtained were sub-sampled by the collection of a few ml of the solution. The sub-samples were kept at 4°C for microscopy analysis to avoid micro-organisms development during storage. As demonstrated by Tamrat et al. (2019)[32], this procedure creates nanoCLICs, which is why these two coprecipitates obtained from basalt and labradorite weathering solutions were called nanoCLICs$_{Basalt}$ and nanoCLICs$_{Labradorite}$.

2.2. Natural soil fine fraction preparation

Natural soil was sampled on the island of Réunion, on the western side of the Piton des Neiges shield volcano, 1720 m ASL (55°21.530 E, 21°04.700 S). The mean annual temperature and precipitation are 13°C and 1,700 mm. The soil supports a forest composed predominantly of tamarinds (*Acacia heterophylla*), philippia (mainly *Philippia montana*), ferns (*Histiapteris incisa*) and bamboo (*Nastus borbonicus*). As a result of intermittent volcanic activity, this soil is an Andosol and consists of a modern surface layer overlying a series of buried horizons. We selected the sil-andic 4Bw horizon (90-190 cm depth, charcoal age of around 40 000 BP) for its high content in low-crystalline phases associated with organic matter[9,29]. X ray diffraction on this horizon previously showed the predominant content of low-crystalline amorphous phase, with some gibbsite and feldspar[9]. Low-crystalline amorphous phases have been characterized by indirect spectroscopic techniques, showing a lower degree of polymerization than imogolites, then referring to proto-imogolites in the papers by Basile-Doelsch et al. (2005, 2007)[9,43] and Levard et al. (2012) [30]. The previous characterization of this horizon showed that it contains 60 gC.kg^{-1} and had a pH of 5.2[9].

176 The soil fine fraction was isolated as follows, in order to isolate them by a slight
177 disaggregation but without modifying the coprecipitates' structure: up to 2 g of humid soil was
178 dispersed in 100 ml of water by sonication (16 $J.ml^{-1}$ by immersion probe; in an ice bath). After
179 48 h of decantation, the supernatant brown gel, enriched in coprecipitates was collected and few
180 µL were immediately deposited on microscopy grids and air-dried.

181 ### 2.3. TEM imaging, TEM-EDX and TEM-EELS chemical maps

182 Solutions containing synthetic nanoCLICs or soil fine fractions were diluted with ultrapure
183 water, at 1/50 and 1/100 ratio, respectively, to limit the number of particles likely to clump
184 together on microscopy grids. Then 7 µL of the sample solutions were directly deposited on a
185 copper grid coated with a Lacey carbon film and air dried. This type of grid allowed us to
186 investigate the structure and chemical compositions of particles located on the holes to prevent C
187 signal from the Lacey C film.

188 Microscopic analyses were performed on and FEI OSIRIS transmission electron microscope
189 (TEM) operating at 200 kV. TEM was used to image the sample from the micrometer to the
190 nanoscale. The scanning transmission electron microscopy configuration was used to image the
191 sample with a very resolved probe size of 1.8 Å and a 0.3 nA current. Two chemical mapping
192 techniques were used in STEM configuration, as detailed hereafter and in SI2, i.e. energy
193 dispersive X-ray spectroscopy (EDX) and electron energy loss spectroscopy (EELS) techniques.

194 • Following electron beam scanning, EDX mapping uses the energy of photons emitted
195 by a volume of the surface sample. EDX at 200 kV allows a wide range of elemental
196 detection. In our study, we focused on C, N, Si, Al, Fe, Ca, K and Mg. However, the
197 exact size of elementary collocations depends on the volume of interaction between

198 the electrons and the material. This volume is hard to estimate, but in STEM mode, it
199 can be about 10 nm[36,37]. Yet the acquisition time necessary to obtain an exploitable
200 signal-to-noise ratio to compute the atomic proportions (at.%) remains long at the 10
201 mn scale, hence, atomic proportions are obtained in areas of several hundred 100 x
202 100 nm. The data were analyzed using Esprit software version 1.9 and atomic
203 proportions were calculated using the PB-ZAF interactive algorithm.

204 • Following the electron beam scan, EELS mapping uses the energy loss of the
205 transmitted electron beam to detect elements. This technique allows us to attribute a
206 very resolved elemental colocation size from a few Å to the nm scale, but the
207 sensitivity is weak for heavy elements (Egerton 2011). This technique allows
208 elementary detection on a range of up to 2000 eV. This range covers the C K-edge
209 (284 eV), O K-edge (532 eV), Fe L-edge (708 eV), Al K-edge (1560 eV) and Si
210 K-edge (1839 eV). However, this technique is more sensitive to light elements (e.g.
211 more sensitive to C K-edge detection than to Si K-edge detection), so it may
212 underestimate heavier elements such as Si[35]. The analysis time per pixel is reduced as
213 much as possible to reduce beam damage, while ensuring elemental detection at the
214 desired scales. EELS ranging from 250 to 1224 eV were acquired first with a pixel
215 analysis time of 0.05 to 0.09 s. In a second step, EELS were acquired from 1,050 to
216 2,074 eV with a time analysis of 0.1 to 1.5 s per pixel. However, due to the potential
217 alterations to elemental fine structure resulting from beam damage [45,46], element
218 speciation is not interpreted in this paper. Data interpretation was done to obtain
219 spatially resolved elemental detection (e.g. extracted core loss signal). EELS data
220 were analyzed using Digital Micrograph software (version 2.32.888.0) and atomic

proportions calculated with power low fitted backgrounds and Hartree Slater cross sections. Energy ranges for power low fitted backgrounds and Hartree Slater cross sections are summarized in SI3.

EDX and EELS mappings are used as complementary methods rather than for comparative purposes, as the thicknesses of the probed zones are unknown (and variable). Furthermore performing EDX and EELS maps can lead to C deposition on the sample (electron-induced carbon fixation from residual gases and local volatilization and re-adsorption from and onto the sample)[47]. To quantify these possible deposits, we synthesized coprecipitates from basalt weathering solution without the addition of DOPA (referred to SRO_{Basalt}), which therefore did not contain C. The EDX and EELS maps showed that the C atomic proportion was low (0.1-0.2%; SI4). Hence, the C deposits were considered negligible under the analysis conditions used. Moreover, TEM imaging, EDX and EELS mappings were carried out in chronological order, but on different particles to avoid any artifacts induced by the preceding analyses.

2.4. Nanoscale elemental colocation using EELS maps

As explained above, the EELS technique allows elemental detection down to a few nm. In order to analyze the elemental colocations of C with inorganic elements at the nanometer scale, we detected the presence or absence of C, Fe, Al and Si elements in each pixel of about 10 nm (pixel lateral distance) of the EELS maps. To automatically perform these elementary multi-detections per pixel, we encoded a script in Python 3.9 that included the following steps: Localization of the elementary thresholds of C K-edge, O K-edge, Fe L-edge, Al K-edge and Si K-edge. Then a power law function fits and removes the background per elementary threshold, as defined by Egerton (2011)[35]. The energy range of the power law fits are mentioned in part

243 SI4. Then elementary detection was done by computing the signal-to-noise ratio (SNR) adapted
244 from Egerton (2011)[35]. The calculations are outlined in SI3. Finally, the script compiles all
245 elementary multi-detections per pixel into a spreadsheet.

246 ## 3. RESULTS

247 ### 3.1. Transmission electron microcopy (TEM) imaging

248 TEM imaging of nanoCLICs$_{Basalt}$ and nanoCLICs$_{Labradorite}$ (Figure 2; SI5) showed that they
249 had a gel-like texture. No crystal planes were detected at the scale of a few nm using high
250 resolution TEM. A fast Fourier transform (FFT) of the images at 10 nm scale did not show any
251 diffraction pattern (indicated by bright dots), thereby suggesting the absence of crystal lattices
252 (Figure 2). The local synthetic nanoCLICs structures were then very similar to each other and
253 characterized as a gel-texture electron-amorphous phase. Moreover, TEM images of the Andosol
254 fine fractions showed close similarities with the synthetic nanoCLICs—these fine fractions were
255 mainly composed of a gel-textured phase (Figure 2) that was also electron amorphous (no atomic
256 arrangement noted at the nanoscale by FFT). However, at microscale, Andosol fine fractions
257 appeared to have greater differences in thickness or density than synthetic nanoCLICs (wider
258 gray-scale contrast for Andosol fine fractions at microscale, Figure 2 and SI5). These differences
259 may also be partly induced by sample preparation (dilution and drying, method 2.3).
260 Furthermore, these analyses showed that these fine Andosol fractions did not have imogolite- or
261 allophane-like arrangements.

262

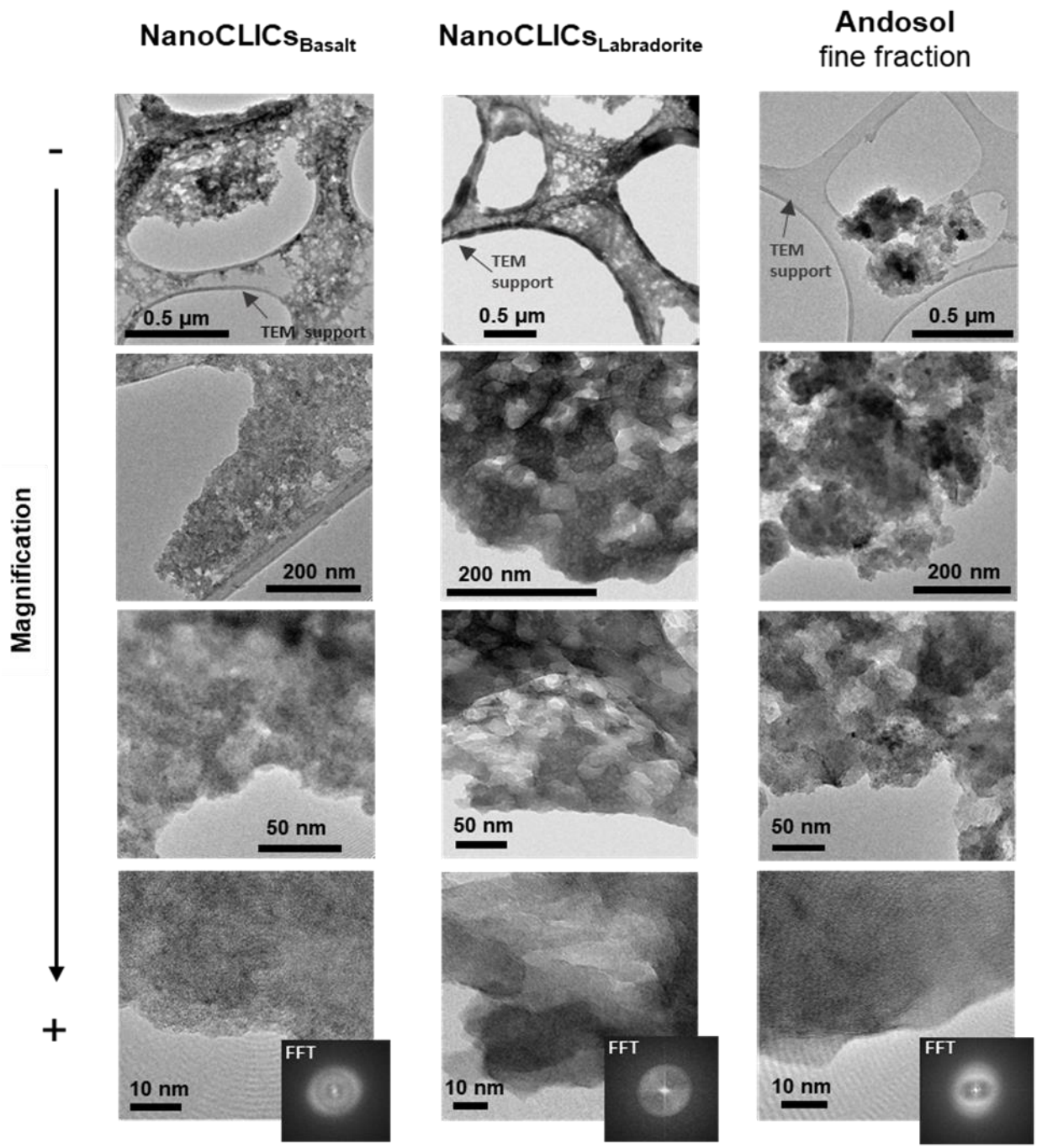

Figure 2. Imaging and characterization of the structure of synthetic nanoCLICs and AAndosol fine fractions using transmission electron microscopy (TEM). Scales range from the micrometer scale to a few nanometers (high-resolution TEM). On high-resolution TEM images (10 nm scale), the fast Fourier transform (FFT) shows electron diffractions characteristic of amorphous structures for synthetic nanoCLICs and for the Andosol fine fraction.

3.2. Energy dispersive x-ray (EDX) mappings

Chemical EDX mappings of nanoCLICs$_{Basalt}$ and nanoCLICs$_{Labradorite}$ revealed a homogeneous distribution of C across the analyzed areas (Figure 3A; SI6). However, C was not detected alone, i.e., Al, Fe and Si were also jointly detected in all of the EDX maps. These inorganic elements (Al, Fe and Si) were also homogeneously distributed in the sample and did not form inorganic clusters. However, nanoCLICs$_{Basalt}$ and nanoCLICs$_{Labradorite}$ had different inorganic compositions when colocalized with C (Figure 3B): nanoCLICs$_{Basalt}$ showed C colocation (59 at.%) with mostly Al (13 at.%), Fe (9 at.%) and Si (7 at.%) whereas nanoCLICs$_{Labradorite}$ had C colocation (32 at.%) with mostly Al (33 at.%) and Si (23 at.%) and trace of Fe (0.3 at.%). These proportions demonstrated that coprecipitates could be formed with different inorganic elements derived from mineral weathering and that the presence of Fe is not necessary for nanoCLICs formation. Moreover, nanoCLICs$_{Basalt}$ and nanoCLICs$_{Labradorite}$ detections revealed other elements, including K, Ca and Mg, but their elemental proportions were negligible (1–3 at.%). Chemical maps of the Andosol fine fractions by EDX also showed that C was heterogeneously detected throughout the sample with Al, Si ad Fe (Figure 3A). Overall, C (45 at.% ; Figure 3B) was colocalized with Al (26 at.%) and Si (19 at.%) and Fe (5 at.%), but unlike the synthetic nanoCLICs, elemental proportions were more spatially heterogeneous—some areas had a higher proportion of Al and Si (sub-area 1; Fe = 3 at.%), while others had more Fe, Al and Si (sub-areas 2 and 3; Fe = 8-9 at.%) and some areas had a lower proportion of C (sub-area 1; C = 24 at.%). In these sub-areas, the three predominant elements in the coprecipitate structures were C (24–42 at.%), Al (20–40 at.%) and Si (18–24 at.%).

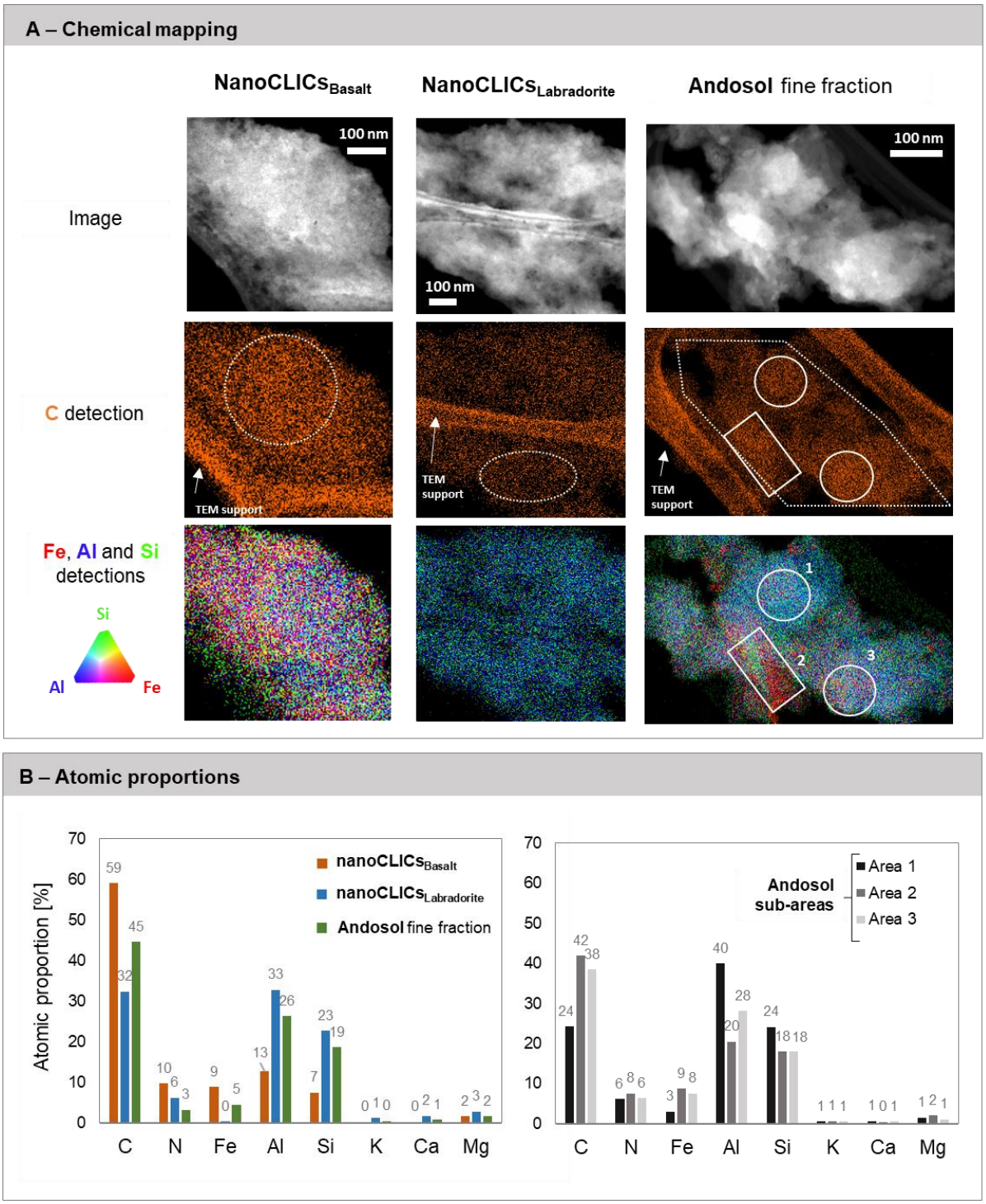

292 **Figure 3.** Chemical mapping of synthetic nanoCLICs and AAndosol fine fractions using STEM-
293 EDX. (A) imaging using a high angular dark field detector and chemical mapping showing
294 elemental detection of C, Fe, Al and Si. (B) The atomic proportions on each sample are from an
295 area of ~0.07 µm², dotted shapes on (A); atomic proportions on sub-areas of AAndosol fine

fractions are shown with a solid line on (A); The proportions do not include O2 and Cu. The acquisition pixel size is of 4, 3 and 1 nm for nanoCLICs$_{Basalt}$, nanoCLICs$_{Labradorite}$ and the AAndosol fine fraction, respectively. Spectra used for atomic proportions are available in SI6.

3.3. Electron energy loss spectroscopy (EELS) mappings

Chemical EELS mapping results of NanoCLICs$_{Basalt}$ and nanoCLICs$_{Labradorite}$ were similar to those obtained by EDX maps**,** i.e. an homogeneous distribution of C throughout all of the analyzed areas and colocation of C with Al, Si and Fe down to the pixel scale (7-11 nm) (Figure 4A; SI7). NanoCLICs$_{Basalt}$ showed C colocation (53 at.%) with mostly Al (16 at.%), Fe (24 at.%) and Si (8 at.%), while nanoCLICs$_{Labradorite}$ had C colocation (39 at.%) with mostly Al (34 at.%) and Si (24 at.%) and little Fe (3 at.%). EELS maps results of the fine Andosol fractions were similar to those obtained by EDX maps, i.e. an heterogeneous detection of C throughout the sample (54 at.%), colocalized with Al (23 at.%), Si (15 at.%), and Fe (7 at.%). However, the elementary colocation proportions were noticeably heterogeneous (sub-areas 4-6), with sub-area 4 rich in Fe (35 at.%) but it also included C (27 at.%), Al (22 at.%) and Si (15 at.%), while sub-area 5 included a C-rich mixture (66 at.%) with Al (15 at.%), Si (10 at.%) and Fe (9 at.%), and sub-area 6 included C-rich mixture (54 at.%) with Al (26 at.%), and Si (16 at.%) and little Fe (3 at.%).

At the nanometer scale of a single pixel (here from 6 to 10 nm of the lateral distance), the signal-to-noise ratio was too low to compute the atomic proportions. However, in a given pixel, we were able to obtain binary information (presence or absence of an element; method used outlined in part 5.4, SI3 and SI8). The inorganic element(s) colocated with C at 6-10 nm scales are summarized in Figure 5. The nanoCLICs$_{Basalt}$ results showed that 94% of C colocalized with

Fe+Al+Si. Little C was measured alone or just with Al or Fe at ~10 nm scale. Otherwise nanoCLICs$_{Labradorite}$ showed that C was predominantly colocalized with Al alone (48%) and Al+Si (37%). Little C was measured alone (9%) at ~10 nm scale. Moreover, the Andosol fine fraction results showed that C was mostly colocalized with mixtures of inorganic elements in decreasing proportion, i.e. Al+Si (32%) > Al+Fe+Si (19%) >Al+Fe (19%) > Al (17%) > Fe+Si (2%) > Si (1%). Consistent with the synthetic nanoCLICs findings, little C was measured alone (6%) in the AAndosol fine fraction at the ~10 nm scale.

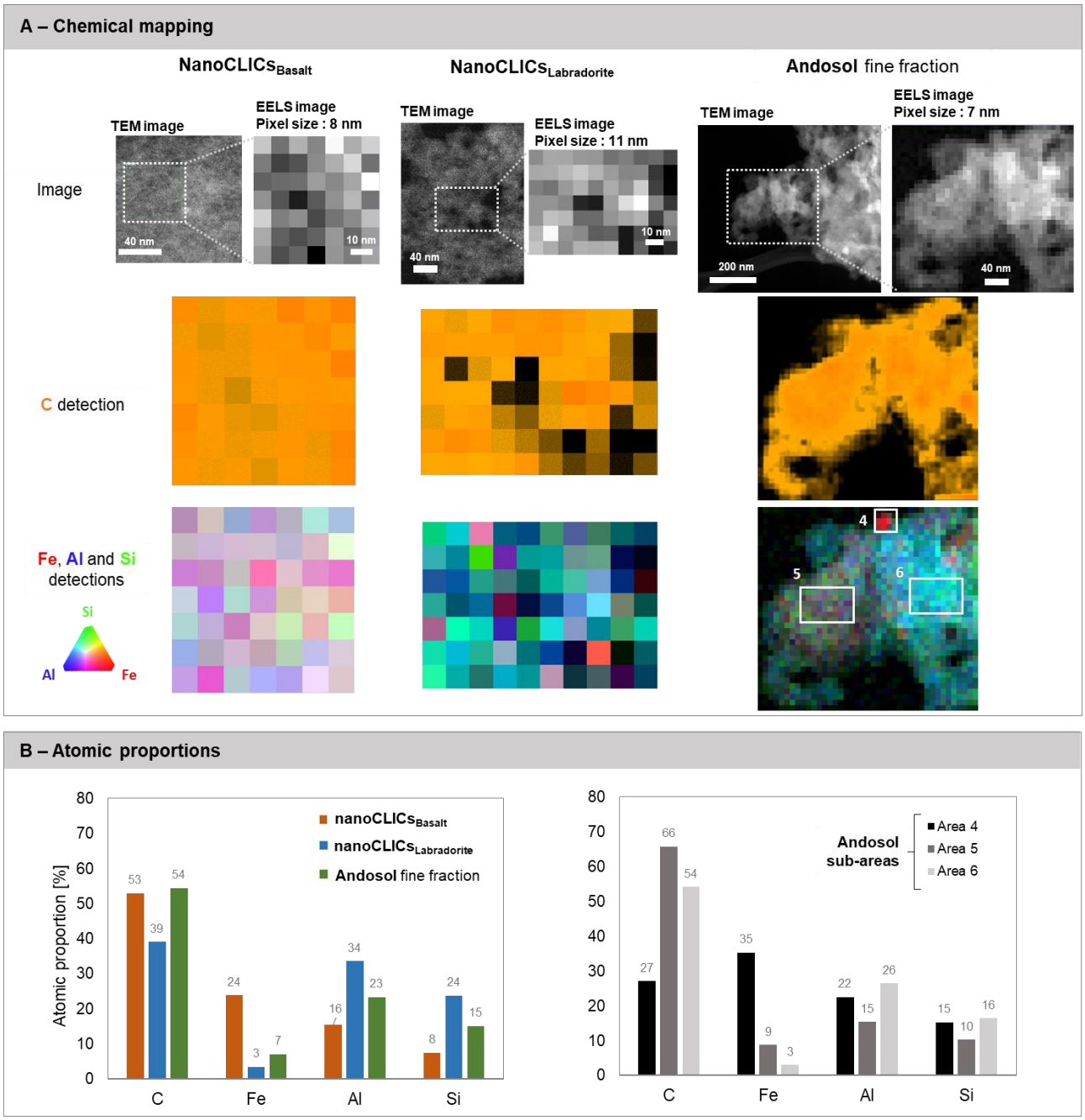

327

328 **Figure 4.** Chemical mapping of synthetic nanoCLICs and Andosol fine fractions using STEM-
329 EELS. (A) image using an angular dark field detector and chemical mapping showing elemental
330 detection of C, Fe, Al and Si. (B) Atomic proportions per sample on the whole images and
331 atomic proportions on sub-areas of the AAndosol fine fraction (sub-areas displayed with solid

lines). The proportions do not take oxygen into account. The acquisition pixel size was 8, 11 and 7 nm for nanoCLICs$_{Basalt}$, nanoCLICs$_{Labradorite}$ and AAndosol fine fractions, respectively. Spectra used for atomic proportion calculation are available in SI7.

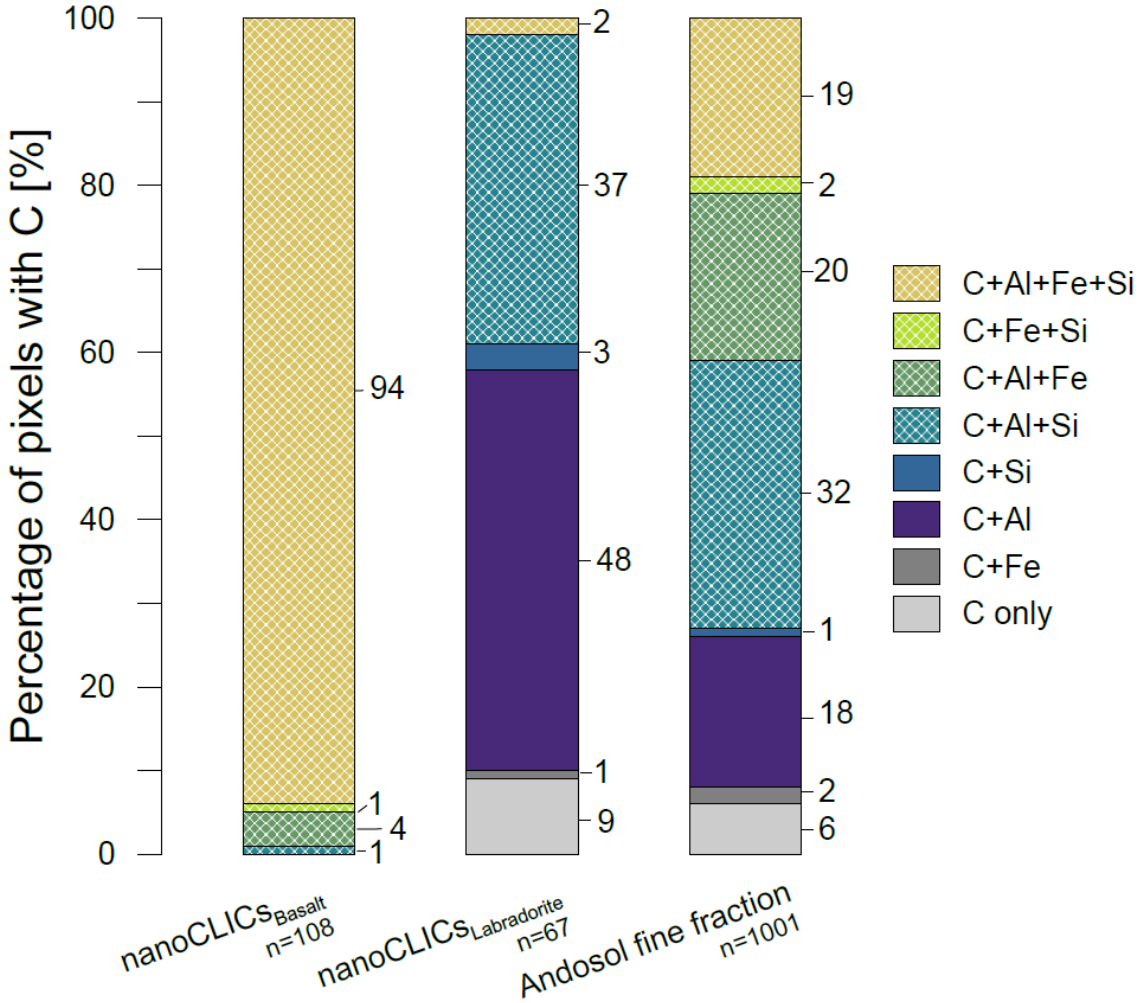

Figure 5. Nanoscale elemental colocalization through EELS mapping of 6-10 nm pixels size. The pixel sizes ranged from 6 to 11 nm (lateral distance). n stands for the number of analyzed pixels with C detection. For each sample, two EELS maps were acquired, this histogram summed the pixels of these two maps (including the EELS shown in Figure 4). A bar chart for each EELS map is shown in Figure SI8. This compilation includes 49 pixels of 8 nm (lateral distance) and 64 pixels of 6 nm for the nanoCLIC$_{basalt}$, 20 pixels of 10 nm and 70 pixels of 11 nm

for the nanoCLICs$_{labradorite}$ and 276 pixels of 10 nm and 1517 pixels of 7 nm for the Andosol fine fraction.

4. DISCUSSION

4.1. First nanoCLICs model results on synthetic coprecipitates with multi-elemental solutions.

The nanoCLICs model proposed by Tamrat et al.[32] (Figure 1) describes coprecipitates in which organic molecules are bound (by covalent or weak bonds) to oligomers of 2-3 inorganic atoms (Fe, Al, Si) structured in a loose irregular 3D network. The representation of this 3D structure was deduced from EXAFS spectroscopy measurements and could be roughly 5 nm in size. For the coprecipitates obtained from the basalt and labradorite weathering solutions, the TEM approaches used in the present study helped validate this nanoCLICs structure model based on the following results. Firstly, the chemical mappings with ~10 nm-pixel-size (from 6 to 8 nm size for nanoCLICs$_{basalt}$ and from 10 to 11 nm size for nanoCLICs$_{Labradorite}$) detected C in majority (91–100%) along with one or more inorganic elements (Al, Si, Fe, see Figures 3, 4 and 5). Furthermore, the electron diffraction results (Figure 2) indicated that the atoms formed an amorphous phase (hence without any electron-detectable crystalline arrangement). The nanoCLICs model results regarding the size, composition or crystal structure criteria were thus consistent for coprecipitates formed from the basalt and labradorite weathering solutions. Yet beyond their common structure, nanoCLICs$_{Basalt}$ and nanoCLICs$_{Labradorite}$ were not identical in all aspects. Prior to coprecipitation, basalt and labradorite weathering solutions contained dissolved Al, Fe and Si, but also Mg and Ca (see Methods, no Fe in labradorite weathering solutions). However, EDX and EELS chemical maps of nanoCLICs$_{Basalt}$ and nanoCLICs$_{Labradorite}$ did not show any substantial presence of Mg and Ca in the synthetic coprecipitates (Figures 3 and 4). These divalent elements thus did not appear to coprecipitate with OM up to pH ~5. A similar trend had also been documented in coprecipitates from biotite weathering within the 4-7 pH range for various OM concentrations[31,32]. Our results confirmed that, regardless of the chemical

371 composition of the initial solution, mono and divalent cations did not enter the synthetic
372 nanoCLICs structure under acidic to neutral conditions. Otherwise, Al, Si and/or Fe were highly
373 present in nanoCLICs$_{Basalt}$ and nanoCLICs$_{Labradorite}$. However, coprecipitation of nanoCLICs$_{Basalt}$
374 was incongruent since, relative to the initial solution, it contained a higher proportion of Al and
375 C, an equivalent or even slightly lower proportion of Fe, but a lower proportion of Si (SI6). In
376 nanoCLICs$_{Labradorite}$, however, the proportions of C, Al and Si present in the solution before
377 coprecipitation remained almost identical in the coprecipitates (SI9), thus reflecting congruent
378 coprecipitation. Based on these results, Figure 6 illustrates the nanoCLICs$_{Basalt}$ and
379 nanoCLICs$_{Labradorite}$ structures which could account for the possible heterogeneity of the
380 inorganic part of the nanoCLICs model (Figure 6). These nanoCLICs models may be used as
381 benchmarks to study, by direct comparison, natural coprecipitates in Andosols.

382

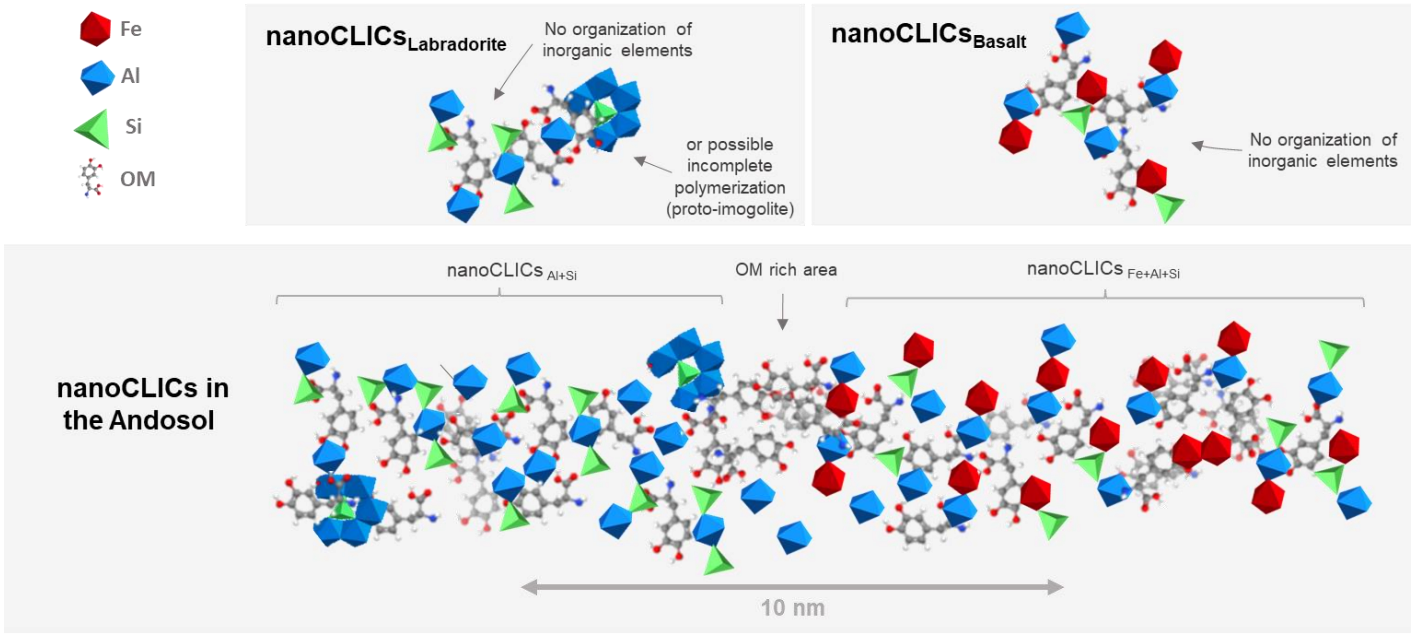

383 **Figure 6.** Conceptual molecular models of nanoCLICs' local structure observed in
384 nanoCLICs$_{Basalt}$, nanoCLICs$_{Labradorite}$ and in the Andosol. For the Andosol fine fraction, note that
385 the model represents an elemental mix of C+Al+Si+Fe or C+Al+Si detected above 10 nm scale.
386 Atomic proportions are deduced from larger-scale analyses from Figure 3 and 4 and should be
387 taken with caution as it is not possible to represent all compositional variability at this scale.
388 Also, organic matter is represented in this scheme by an identical small organic molecule,
389 however, co-precipitated organic matter is most likely heterogeneous in composition and size.

4.2. Coprecipitates in Andosol fine fractions: are they natural nanoCLICs?

The local structure of the inorganic part of the Andosol coprecipitates analyzed in this study was characterized in a previous study[29], highlighting the absence of allophane spheres and imogolite tubes as well as very limited local organization of Al and Si atoms. The authors therefore concluded that the mineral part was likely rather poorly ordered proto-imogolites. Our results confirmed that the Andosol fine fraction consisted of an electron amorphous phase (Figure 2), indicating that the atoms were not organized in a crystallographic lattice. From a local structure perspective, the Andosol fine fraction coprecipitates were therefore very similar to synthetic nanoCLICs in which inorganic elements are structured in a loose irregular 3D structure of small amorphous oligomers forming an amorphous and open-structured mineral skeleton[32]. Otherwise, regarding their elemental composition (from EDX and EELS mappings), the Andosol fine fraction coprecipitates contained C, Al, Fe and Si in proportions quite similar to those of synthetic nanoCLICs (SI9). Our results thus suggested that the natural Andosol coprecipitates were mainly composed of organic molecules bound to an inorganic network of amorphous small oligomers (See SI10 for further clarification). However, it is likely that the organic compounds may also have simply been complexed with unpolymerized Al and Fe (monomers) within the coprecipitates. Figure 6 illustrates the Andosol coprecipitate structures, as done for the nanoCLICs$_{Basalt}$ and nanoCLICs$_{Labradorite}$. In conclusion, the local structure and chemical nature of the Andosol coprecipitates were similar to those of both synthetic coprecipitates (no crystalline structure and elemental mix of C, Al, Si and ±Fe down to 7 nm), thereby showing that the inorganic part that stabilized C in the studied Andosol could be assimilated to nanoCLICs. We hence propose to qualify the Andosol coprecipitates as ‘natural nanoCLICs’.

4.3. Heterogeneity of natural nanoCLICs in Andosol

The EELS and EDX results (Figure 3-6) showed that the composition of natural nanoCLICs was somewhat heterogeneous. For example, the C+Al+Fe+Si mix was mainly located in sub-area 5 (Figure 4), while the C+Al+Si mix was more prevalent in sub-area 6. Several non-exclusive assumptions could be put forward to explain this heterogeneity: (i) It could be the result of coprecipitation from locally different soil solutions since in the two synthetic systems studied we found that the variability of elements present in the starting solution could create nanoCLICs with inorganic phases of different compositions (i.e. Al+Si+Fe for nanoCLICs$_{Basalt}$ and Al+Si or Al only for nanoCLICs$_{Labradorite}$, Figure 5). Indeed, soil solutions can show variations in element concentrations depending on their proximity to different types of minerals of varying chemical compositions; (ii) Soil solution concentration heterogeneity could be related to the extent of weathering of the minerals that provide the dissolved elements, particularly for non-congruent weathered mineral phases[31]; (iii) Also, this degree of mineral weathering could be locally variable depending on the biotic environment of the mineral (presence of root exudates, microorganisms, etc.) and physicochemical (moisture, pH, Eh[48–50]) conditions. For Fe especially, in an Andosol at the micrometer scale, coprecipitates were previously found to have less C collocated with Fe when there were marked redox fluctuations[51,52]. Redox fluctuations might therefore induce Fe migration out of nanoCLICs. Fe could then migrate into re-oxidation clusters, as observed in Figure 4..(iv) Finally, even if the speciation of organic matter could not be probed here, different proportions of C were detected (at the centi-nanometric scale; Figure 3 and 4). These variations could result from different types of organic molecules or matter which have more or less affinities for a given metal, and thus, could give elementary mixture heterogeneities. These multiple factors would likely induce the formation of natural nanoCLICs that could present very small-scale variations in Al, Si and/or Fe composition. In the Andosol,

natural nanoCLICs were thus mainly composed of nanoCLICsC+Al+Si (32%), nanoCLICsC+Al+Si+Fe (19%), nanoCLICsC+Al+Fe (19%), nanoCLICsC+Al (18%). The local variability in natural nanoCLICs is schematically illustrated in 2D in Figure 6, where Al, Si and Fe might play different roles in the organic compound stabilization process.

4.4. Different roles of Fe, Al and Si in organic compound stabilization in nanoCLICs

In the studied Andosol, Fe is not the major element expected to stabilize C in coprecipitates, but rather Al and Si, often described in the form of allophane and imogolites[54,55]. However, a slight amount of Fe is detected in the coprecipitates of this andosol (up to 3 to 8 at.% in Figures 3 and 4, excepted area 4). In literature, Fe has long been identified for its high affinity to organic molecules and put forward as playing a primary function in stabilizing OM in soils [56–59,17,19–21,23,24] as well as in sediments[60,61], and even in some Andosols [62,63]. The short-range order form of Fe, i.e. ferrihydrite (Figure 1), has been widely cited for its high reactivity, mainly related to its large specific surface. This ferrihydrite + OM association was represented by Kleber et al.[3] with an interaction model that showed Fe octahedrons organized in spherical clusters of a few thousand Fe atoms, and these clusters were aggregated together to form Fe oxy-hydroxide phases of several tens of nanometers[3]. In the Andosol studied here, despite the presence of Fe, the TEM maps did not highlight any such high Fe-rich zones over several tens of nanometers. Moreover, the proportion of pixels in which C was only associated with Fe was very small (2%). Hence, we concluded that Fe in form of ferrihydrite was not involved in the Andosol fine fraction stabilization process. Most of the Fe was associated with Al or Si and the rest was locally more concentrated in some areas (area 2 in Figure 3, areas 2 and 4 in Figure 4). This indicates that, despite the fact that Fe was not expected in the coprecipitate of this andosol, it is important when it is associated in nanoscale elementary mixtures as Fe+Al+Si, Fe+Al and Fe+Si (41% of the ~10

nm pixels had Fe+Al+Si, Fe+Al and Fe+Si detections). Similar results were obtained by NanoSIMS on ferromanganese concretions in a Stagnosol[53]. These authors showed that Fe and C were not necessarily collocated at the submicron scale, confirming the necessity of spatially resolved studies along with, a more frequent than previously thought, decoupling of Fe and organic matter. As for Fe, Al has also long been recognized for its affinity to organic molecules[64,65,28]. Our results showed that Al appeared to play a major role in stabilizing organic matter in Andosol fine fractions. Indeed, Al was colocalized with C in 89% of the pixels (Figure 5). 18% of the pixels showed colocation of C with Al alone. Al associated with C was also mainly associated with Si (32%), with an Al/Si ratio of close to 2, potentially in a proto-imogolite type of structure as described previously[29]. Yet Al was also associated with Fe in the presence (19%) or absence (20%) of Si. However, Si detection was probably underestimated by EELS mapping (see Methods). Al hence appeared to play a central role in interactions with OM within Andosol natural nanoCLICs. Unlike Al and Fe, Si is known to have low affinity to OM[66]. However, it was present to a substantial extent in the structure of nanoCLICs and, in most of the nanoCLICs analyzed (except for nanoCLICs$_{Basalt}$), in a larger proportion than Fe. The presence of Si in coprecipitates is described as being a factor that disrupts Al and Fe oxy-hydroxide polymerization, thereby preventing their crystal growth into gibbsite, ferrihydrite or goethite[67–69,9,43,70]. The presence of Si could therefore maintain amorphous Al and Fe structures in the oligomeric state, hence ensuring greater accessibility of reactive OH groups[70]. Si would favor the preservation of the very poorly polymerized state, maintaining the high specific surface area and high reactivity of the inorganic skeleton of nanoCLICs[32]. Si would also limit the progressive aging of Fe (and Al) phases towards better crystallized and more stable Fe (and Al) oxides[71], thereby ensuring OM stabilization within natural nanoCLICs.

5. ENVIRONMENTAL IMPLICATIONS

The findings of this study showed that, using solutions containing various elements, the coprecipitates formed are of the nanoCLICS type and so even less organized than SRO-OM usually described. Thus, depending on the element concentrations and pH levels of these solutions, the amorphous nanoCLICs-type of coprecipitates are likely to be formed in many types of soils and environments at pH ~4–6, and not SRO-OM, as usually conceptualized in the literature. In addition to their potential presence, their amorphous structure might lead to their rapid fluctuations in ecosystems. In soils, the physicochemical conditions of a microsite can change over time, especially in the rhizosphere [72–75]. These changes disrupt some organo-mineral associations and thereby allow access to OM (and thus nutrients as Fe and Si) previously unavailable to microorganisms and plants. This sensitivity to disruption is higher for organo-mineral associations with a lower crystalline inorganic part[76]. Considering the amorphous and heterogeneous nature of the inorganic part of nanoCLICs, nanoCLICs could be fairly unstable in soil microsites and subject to disruption, particularly in the rhizosphere. NanoCLICs could thus have a predominant role in plant and microorganism nutrient cycles. Moreover, the role of coprecipitates has recently been highlighted in the maintenance of soil aggregates via their glue-like properties[77,78]. By their gel-like texture observed in this study, nanoCLICs could also be involved in soil aggregate formation. However, nanoCLICs are hard to detect because it depends on costly nanoscale analytical methods (hard to extrapolate to large scales). Despite these obstacles, future research could be geared towards quantifying nanoCLICs in various environments to gain further insight into their importance in rapid soil C stock dynamics, as well as in other environments such as sediments.

ASSOCIATED CONTENT

Supporting Information

SI 1. Measurement of dissolved elements in the basalt and labradorite weathering solutions obtained by ICP-AES.

SI 2. Table of microscopic analysis parameters used for TEM imaging and chemical mapping.

SI 3. Determination of the signal-to-noise ratio for the detection of C, O, Fe, Al and Si elements per pixel.

SI 4. C contamination survey: EDX and EELS mapping on SRO_{Basalt}.

S I5. TEM images and EDX and EELS mapping summary.

SI 6. EDX spectra used in Figure 3 for atomic proportions.

SI 7. EELS spectra used in Figure 4 for atomic proportions.

SI 8. Summary of the acquired EELS data and bar plot of all acquired EELS maps with a lateral pixel size of 6-10 nm.

SI 9. Comparison of atomic proportions between Al-Fe-Si and Al-Fe-C before coprecipitation and in the $nanoCLICs_{Basalt}$, $nanoCLICs_{Labradorite}$ and the Andosol fine fraction.

SI 10. Detailed information to interpret the inorganic part of co-precipitates as predominantly oligomers.

Funding Sources

ANR (NanoSoilC project ANR-16-CE01-0012-02), the Equipex nanoID platform (2010-2019), la Région SUD and CIRAD (Emploi Jeunes Doctorants, subvention n°2019_03559, DEB 19-574).

Notes

Data is available upon request to the corresponding author. The code used for nanoscale elemental colocation through EELS mapping is available at the following link: https://github.com/FlorianeJamoteau/EELS_elemental_detection_and_multi-detections.

ACKNOWLEDGMENT

We would like to thank the research funding partners: ANR (NanoSoilC project ANR-16-CE01-0012-02), the Equipex nanoID platform (2010-2019), la Région SUD and CIRAD (Emploi Jeunes Doctorants, subvention n°2019_03559, DEB 19-574). We thank Jérôme Rose who headed the Equipex nanoID platform that was used for the microscopy analyses.

REFERENCES

(1) Friedlingstein, P.; O'Sullivan, M.; Jones, M. W.; Andrew, R. M.; Gregor, L.; Hauck, J.; Le Quéré, C.; Luijkx, I. T.; Olsen, A.; Peters, G. P.; Peters, W.; Pongratz, J.; Schwingshackl, C.; Sitch, S.; Canadell, J. G.; Ciais, P.; Jackson, R. B.; Alin, S. R.; Alkama, R.; Arneth, A.; Arora, V. K.; Bates, N. R.; Becker, M.; Bellouin, N.; Bittig, H. C.; Bopp, L.; Chevallier, F.; Chini, L. P.; Cronin, M.; Evans, W.; Falk, S.; Feely, R. A.; Gasser, T.; Gehlen, M.; Gkritzalis, T.; Gloege, L.; Grassi, G.; Gruber, N.; Gürses, Ö.; Harris, I.; Hefner, M.; Houghton, R. A.; Hurtt, G. C.; Iida, Y.; Ilyina, T.; Jain, A. K.; Jersild, A.; Kadono, K.; Kato, E.; Kennedy, D.; Klein Goldewijk, K.; Knauer, J.; Korsbakken, J. I.; Landschützer, P.; Lefèvre, N.; Lindsay, K.; Liu, J.; Liu, Z.; Marland, G.; Mayot, N.; McGrath, M. J.; Metzl, N.; Monacci, N. M.; Munro, D. R.; Nakaoka, S.-I.; Niwa, Y.; O'Brien, K.; Ono, T.; Palmer, P. I.; Pan, N.; Pierrot, D.; Pocock, K.; Poulter, B.; Resplandy, L.; Robertson, E.; Rödenbeck, C.; Rodriguez, C.; Rosan, T. M.; Schwinger, J.; Séférian, R.; Shutler, J. D.; Skjelvan, I.; Steinhoff, T.; Sun, Q.; Sutton, A. J.; Sweeney, C.; Takao, S.; Tanhua, T.; Tans, P. P.; Tian, X.; Tian, H.; Tilbrook, B.; Tsujino, H.; Tubiello, F.; van der Werf, G. R.; Walker, A. P.; Wanninkhof, R.; Whitehead, C.; Willstrand Wranne, A.; Wright, R.; Yuan, W.; Yue, C.; Yue, X.; Zaehle, S.; Zeng, J.; Zheng, B. Global Carbon Budget 2022. *Earth System Science Data* **2022**, *14* (11), 4811–4900. https://doi.org/10.5194/essd-14-4811-2022.

(2) Schmidt, M. W. I.; Torn, M. S.; Abiven, S.; Dittmar, T.; Guggenberger, G.; Janssens, I. A.; Kleber, M.; Kögel-Knabner, I.; Lehmann, J.; Manning, D. A. C.; Nannipieri, P.; Rasse, D. P.; Weiner, S.; Trumbore, S. E. Persistence of Soil Organic Matter as an Ecosystem Property. *Nature* **2011**, *478* (7367), 49–56. https://doi.org/10.1038/nature10386.

(3) Kleber, M.; Eusterhues, K.; Keiluweit, M.; Mikutta, C.; Mikutta, R.; Nico, P. S. Chapter One - Mineral–Organic Associations: Formation, Properties, and Relevance in Soil Environments. In *Advances in Agronomy*; Sparks, D. L., Ed.; Academic Press, 2015; Vol. 130, pp 1–140. https://doi.org/10.1016/bs.agron.2014.10.005.

(4) Stoner, S. W.; Schrumpf, M.; Hoyt, A. M.; Sierra, C. A.; Doetterl, S.; Galy, V.; Trumbore, S. How Well Does Ramped Thermal Oxidation Quantify the Age Distribution of Soil Carbon? Assessing Thermal Stability of Physically and Chemically Fractionated Soil Organic Matter. *EGUsphere* **2022**, 1–23. https://doi.org/10.5194/egusphere-2022-624.

(5) Hemingway, J. D.; Rothman, D. H.; Grant, K. E.; Rosengard, S. Z.; Eglinton, T. I.; Derry, L. A.; Galy, V. V. Mineral Protection Regulates Long-Term Global Preservation of Natural Organic Carbon. *Nature* **2019**, *570* (7760), 228–231. https://doi.org/10.1038/s41586-019-1280-6.

(6) Balesdent, J.; Basile-Doelsch, I.; Chadoeuf, J.; Cornu, S. S.; Derrien, D.; Fekiacova, Z.; Hatté, C. Atmosphere–Soil Carbon Transfer as a Function of Soil Depth. *Nature* **2018**, *559* (7715), 599–602. https://doi.org/10.1038/s41586-018-0328-3.
(7) Shi, Z.; Allison, S. D.; He, Y.; Levine, P. A.; Hoyt, A. M.; Beem-Miller, J.; Zhu, Q.; Wieder, W. R.; Trumbore, S.; Randerson, J. T. The Age Distribution of Global Soil Carbon Inferred from Radiocarbon Measurements. *Nat. Geosci.* **2020**, *13* (8), 555–559. https://doi.org/10.1038/s41561-020-0596-z.
(8) Kleber, M.; Bourg, I. C.; Coward, E. K.; Hansel, C. M.; Myneni, S. C. B.; Nunan, N. Dynamic Interactions at the Mineral–Organic Matter Interface. *Nat Rev Earth Environ* **2021**, *2* (6), 402–421. https://doi.org/10.1038/s43017-021-00162-y.
(9) Basile-Doelsch, I.; Amundson, R.; Stone, W. E. E.; Masiello, C. A.; Bottero, J. Y.; Colin, F.; Masin, F.; Borschneck, D.; Meunier, J. D. Mineralogical Control of Organic Carbon Dynamics in a Volcanic Ash Soil on La Réunion. *European Journal of Soil Science* **2005**, *56* (6), 689–703. https://doi.org/10.1111/j.1365-2389.2005.00703.x.
(10) Finlay, R. D.; Mahmood, S.; Rosenstock, N.; Bolou-Bi, E. B.; Köhler, S. J.; Fahad, Z.; Rosling, A.; Wallander, H.; Belyazid, S.; Bishop, K.; Lian, B. Reviews and Syntheses: Biological Weathering and Its Consequences at Different Spatial Levels – from Nanoscale to Global Scale. *Biogeosciences* **2020**, *17* (6), 1507–1533. https://doi.org/10.5194/bg-17-1507-2020.
(11) Kramer, M. G.; Chadwick, O. A. Climate-Driven Thresholds in Reactive Mineral Retention of Soil Carbon at the Global Scale. *Nature Clim Change* **2018**, *8* (12), 1104–1108. https://doi.org/10.1038/s41558-018-0341-4.
(12) Rasmussen, C.; Heckman, K.; Wieder, W. R.; Keiluweit, M.; Lawrence, C. R.; Berhe, A. A.; Blankinship, J. C.; Crow, S. E.; Druhan, J. L.; Hicks Pries, C. E.; Marin-Spiotta, E.; Plante, A. F.; Schädel, C.; Schimel, J. P.; Sierra, C. A.; Thompson, A.; Wagai, R. Beyond Clay: Towards an Improved Set of Variables for Predicting Soil Organic Matter Content. *Biogeochemistry* **2018**, *137* (3), 297–306. https://doi.org/10.1007/s10533-018-0424-3.
(13) Blakemore, L. C. Methods for Chemical Analysis of Soils. *N.Z.Soil Bureau Scientific Report* **1987**, *80*, 71–76.
(14) Rennert, T. Wet-Chemical Extractions to Characterise Pedogenic Al and Fe Species – a Critical Review. *Soil Res.* **2018**, *57* (1), 1–16. https://doi.org/10.1071/SR18299.
(15) Vilgé-Ritter, A.; Rose, J.; Masion, A.; Bottero, J.-Y.; Lainé, J.-M. Chemistry and Structure of Aggregates Formed with Fe-Salts and Natural Organic Matter. *Colloids and Surfaces A: Physicochemical and Engineering Aspects* **1999**, *147* (3), 297–308. https://doi.org/10.1016/S0927-7757(98)00325-2.
(16) Schwertmann, U.; Wagner, F.; Knicker, H. Ferrihydrite–Humic Associations. *Soil Science Society of America Journal* **2005**, *69* (4), 1009–1015. https://doi.org/10.2136/sssaj2004.0274.
(17) Mikutta, C.; Mikutta, R.; Bonneville, S.; Wagner, F.; Voegelin, A.; Christl, I.; Kretzschmar, R. Synthetic Coprecipitates of Exopolysaccharides and Ferrihydrite. Part I: Characterization. *Geochimica et Cosmochimica Acta* **2008**, *72* (4), 1111–1127. https://doi.org/10.1016/j.gca.2007.11.035.
(18) Karlsson, T.; Persson, P.; Skyllberg, U.; Mörth, C.-M.; Giesler, R. Characterization of Iron(III) in Organic Soils Using Extended X-Ray Absorption Fine Structure Spectroscopy. *Environ Sci Technol* **2008**, *42* (15), 5449–5454. https://doi.org/10.1021/es800322j.

(19) Karlsson, T.; Persson, P. Coordination Chemistry and Hydrolysis of Fe(III) in a Peat Humic Acid Studied by X-Ray Absorption Spectroscopy. *Geochimica et Cosmochimica Acta* **2010**, *74*, 30–40. https://doi.org/10.1016/j.gca.2009.09.023.
(20) Eusterhues, K.; Rennert, T.; Knicker, H.; Kögel-Knabner, I.; Totsche, K. U.; Schwertmann, U. Fractionation of Organic Matter Due to Reaction with Ferrihydrite: Coprecipitation versus Adsorption. *Environ. Sci. Technol.* **2011**, *45* (2), 527–533. https://doi.org/10.1021/es1023898.
(21) Karlsson, T.; Persson, P. Complexes with Aquatic Organic Matter Suppress Hydrolysis and Precipitation of Fe(III). *Chemical Geology* **2012**, *322–323*, 19–27. https://doi.org/10.1016/j.chemgeo.2012.06.003.
(22) Mikutta, R.; Lorenz, D.; Guggenberger, G.; Haumaier, L.; Freund, A. Properties and Reactivity of Fe-Organic Matter Associations Formed by Coprecipitation versus Adsorption: Clues from Arsenate Batch Adsorption. *Geochimica et Cosmochimica Acta* **2014**, *144*, 258–276. https://doi.org/10.1016/j.gca.2014.08.026.
(23) Eusterhues, K.; Neidhardt, J.; Hädrich, A.; Küsel, K.; Totsche, K. U. Biodegradation of Ferrihydrite-Associated Organic Matter. *Biogeochemistry* **2014**, *119* (1), 45–50. https://doi.org/10.1007/s10533-013-9943-0.
(24) Chen, K.-Y.; Chen, T.-Y.; Chan, Y.-T.; Cheng, C.-Y.; Tzou, Y.-M.; Liu, Y.-T.; Teah, H.-Y. Stabilization of Natural Organic Matter by Short-Range-Order Iron Hydroxides. *Environ. Sci. Technol.* **2016**, *50* (23), 12612–12620. https://doi.org/10.1021/acs.est.6b02793.
(25) Possinger, A. R.; Zachman, M. J.; Dynes, J. J.; Regier, T. Z.; Kourkoutis, L. F.; Lehmann, J. Co-Precipitation Induces Changes to Iron and Carbon Chemistry and Spatial Distribution at the Nanometer Scale. *Geochimica et Cosmochimica Acta* **2021**, *314*, 1–15. https://doi.org/10.1016/j.gca.2021.09.003.
(26) Masion, A.; Bertsch, P. M. Aluminium Speciation in the Presence of Wheat Root Cell Walls: A Wet Chemical Study. *Plant, Cell & Environment* **1997**, *20* (4), 504–512. https://doi.org/10.1046/j.1365-3040.1997.d01-86.x.
(27) Masion, A.; Vilgé-Ritter, A.; Rose, J.; Stone, W. E. E.; Teppen, B. J.; Rybacki, D.; Bottero, J.-Y. Coagulation-Flocculation of Natural Organic Matter with Al Salts: Speciation and Structure of the Aggregates. *Environ. Sci. Technol.* **2000**, *34* (15), 3242–3246. https://doi.org/10.1021/es9911418.
(28) Mikutta, R.; Zang, U.; Chorover, J.; Haumaier, L.; Kalbitz, K. Stabilization of Extracellular Polymeric Substances (Bacillus Subtilis) by Adsorption to and Coprecipitation with Al Forms. *Geochimica et Cosmochimica Acta* **2011**, *75* (11), 3135–3154. https://doi.org/10.1016/j.gca.2011.03.006.
(29) Levard, C.; Doelsch, E.; Basile-Doelsch, I.; Abidin, Z.; Miche, H.; Masion, A.; Rose, J.; Borschneck, D.; Bottero, J.-Y. Structure and Distribution of Allophanes, Imogolite and Proto-Imogolite in Volcanic Soils. *Geoderma* **2012**, *183–184*, 100–108. https://doi.org/10.1016/j.geoderma.2012.03.015.
(30) Kleber, M.; Sollins, P.; Sutton, R. A Conceptual Model of Organo-Mineral Interactions in Soils: Self-Assembly of Organic Molecular Fragments into Zonal Structures on Mineral Surfaces. *Biogeochemistry* **2007**, *85* (1), 9–24. https://doi.org/10.1007/s10533-007-9103-5.
(31) Tamrat, W. Z.; Rose, J.; Grauby, O.; Doelsch, E.; Levard, C.; Chaurand, P.; Basile-Doelsch, I. Composition and Molecular Scale Structure of Nanophases Formed by Precipitation of Biotite Weathering Products. *Geochimica et Cosmochimica Acta* **2018**, *229*, 53–64. https://doi.org/10.1016/j.gca.2018.03.012.

(32) Tamrat, W. Z.; Rose, J.; Grauby, O.; Doelsch, E.; Levard, C.; Chaurand, P.; Basile-Doelsch, I. Soil Organo-Mineral Associations Formed by Co-Precipitation of Fe, Si and Al in Presence of Organic Ligands. *Geochimica et Cosmochimica Acta* **2019**, *260*, 15–28. https://doi.org/10.1016/j.gca.2019.05.043.
(33) Weng, Z. (Han); Lehmann, J.; Van Zwieten, L.; Joseph, S.; Archanjo, B. S.; Cowie, B.; Thomsen, L.; Tobin, M. J.; Vongsvivut, J.; Klein, A.; Doolette, C. L.; Hou, H.; Mueller, C. W.; Lombi, E.; Kopittke, P. M. Probing the Nature of Soil Organic Matter. *Critical Reviews in Environmental Science and Technology* **2022**, *52* (22), 4072–4093. https://doi.org/10.1080/10643389.2021.1980346.
(34) Williams, D. B.; Carter, C. B. *Transmission Electron Microscopy*; Springer US: Boston, MA, 2009. https://doi.org/10.1007/978-0-387-76501-3.
(35) Egerton, R. F. *Electron Energy-Loss Spectroscopy in the Electron Microscope*; Springer US: Boston, MA, 2011. https://doi.org/10.1007/978-1-4419-9583-4.
(36) *Introduction to Analytical Electron Microscopy*; Hren, J. J., Goldstein, J. I., Joy, D. C., Eds.; Springer US: Boston, MA, 1979. https://doi.org/10.1007/978-1-4757-5581-7.
(37) Rez, P. A Transport Equation Theory of Beam Spreading in the Electron Microscope. *Ultramicroscopy* **1983**, *12* (1), 29–38. https://doi.org/10.1016/0304-3991(83)90302-9.
(38) Chenu, C.; Plante, A. F. Clay-Sized Organo-Mineral Complexes in a Cultivation Chronosequence: Revisiting the Concept of the 'Primary Organo-Mineral Complex.' *European Journal of Soil Science* **2006**, *57* (4), 596–607. https://doi.org/10.1111/j.1365-2389.2006.00834.x.
(39) Wen, Y.; Li, H.; Xiao, J.; Wang, C.; Shen, Q.; Ran, W.; He, X.; Zhou, Q.; Yu, G. Insights into Complexation of Dissolved Organic Matter and Al(III) and Nanominerals Formation in Soils under Contrasting Fertilizations Using Two-Dimensional Correlation Spectroscopy and High Resolution-Transmission Electron Microscopy Techniques. *Chemosphere* **2014**, *111*, 441–449. https://doi.org/10.1016/j.chemosphere.2014.03.078.
(40) Cornelis, J.-T.; Delvaux, B.; Van Ranst, E.; Rouxhet, P. G. Sub-Micrometer Distribution of Fe Oxides and Organic Matter in Podzol Horizons. *Geoderma* **2018**, *323*, 126–135. https://doi.org/10.1016/j.geoderma.2018.02.043.
(41) Possinger, A. R.; Zachman, M. J.; Enders, A.; Levin, B. D. A.; Muller, D. A.; Kourkoutis, L. F.; Lehmann, J. Organo–Organic and Organo–Mineral Interfaces in Soil at the Nanometer Scale. *Nat Commun* **2020**, *11* (1), 6103. https://doi.org/10.1038/s41467-020-19792-9.
(42) Sutton, R.; Sposito, G. Molecular Structure in Soil Humic Substances: The New View. *Environ. Sci. Technol.* **2005**, *39* (23), 9009–9015. https://doi.org/10.1021/es050778q.
(43) Basile-Doelsch, I.; Amundson, R.; Stone, W. E. E.; Borschneck, D.; Bottero, J. Y.; Moustier, S.; Masin, F.; Colin, F. Mineral Control of Carbon Pools in a Volcanic Soil Horizon. *Geoderma* **2007**, *137* (3), 477–489. https://doi.org/10.1016/j.geoderma.2006.10.006.
(44) Silva, J. H. S.; Deenik, J. L.; Yost, R. S.; Bruland, G. L.; Crow, S. E. Improving Clay Content Measurement in Oxidic and Volcanic Ash Soils of Hawaii by Increasing Dispersant Concentration and Ultrasonic Energy Levels. *Geoderma* **2015**, *237–238*, 211–223. https://doi.org/10.1016/j.geoderma.2014.09.008.
(45) Vesely, D. Electron Beam Damage of Amorphous Synthetic Polymers. *Ultramicroscopy* **1984**, *14* (3), 279–290. https://doi.org/10.1016/0304-3991(84)90096-2.

(46) Libera, M. R.; Egerton, R. F. Advances in the Transmission Electron Microscopy of Polymers. *Polymer Reviews* **2010**, *50* (3), 321–339. https://doi.org/10.1080/15583724.2010.493256.
(47) Bret, T.; Mauron, S.; Utke, I.; Hoffmann, P. Characterization of Focused Electron Beam Induced Carbon Deposits from Organic Precursors. *Microelectronic Engineering* **2005**, *78–79*, 300–306. https://doi.org/10.1016/j.mee.2005.01.006.
(48) Smits, M. M.; Wallander, H. Chapter 3 - Role of Mycorrhizal Symbiosis in Mineral Weathering and Nutrient Mining from Soil Parent Material. In *Mycorrhizal Mediation of Soil*; Johnson, N. C., Gehring, C., Jansa, J., Eds.; Elsevier, 2017; pp 35–46. https://doi.org/10.1016/B978-0-12-804312-7.00003-6.
(49) Samuels, T.; Bryce, C.; Landenmark, H.; Marie-Loudon, C.; Nicholson, N.; Stevens, A. H.; Cockell, C. Microbial Weathering of Minerals and Rocks in Natural Environments. In *Biogeochemical Cycles*; American Geophysical Union (AGU), 2020; pp 59–79. https://doi.org/10.1002/9781119413332.ch3.
(50) Wild, B.; Imfeld, G.; Daval, D. Direct Measurement of Fungal Contribution to Silicate Weathering Rates in Soil. *Geology* **2021**, *49* (9), 1055–1058. https://doi.org/10.1130/G48706.1.
(51) Inagaki, T. M.; Possinger, A. R.; Grant, K. E.; Schweizer, S. A.; Mueller, C. W.; Derry, L. A.; Lehmann, J.; Kögel-Knabner, I. Subsoil Organo-Mineral Associations under Contrasting Climate Conditions. *Geochimica et Cosmochimica Acta* **2020**, *270*, 244–263. https://doi.org/10.1016/j.gca.2019.11.030.
(52) Possinger, A. R.; Bailey, S. W.; Inagaki, T. M.; Kögel-Knabner, I.; Dynes, J. J.; Arthur, Z. A.; Lehmann, J. Organo-Mineral Interactions and Soil Carbon Mineralizability with Variable Saturation Cycle Frequency. *Geoderma* **2020**, *375*, 114483. https://doi.org/10.1016/j.geoderma.2020.114483.
(53) Rennert, T.; Händel, M.; Höschen, C.; Lugmeier, J.; Steffens, M.; Totsche, K. U. A NanoSIMS Study on the Distribution of Soil Organic Matter, Iron and Manganese in a Nodule from a Stagnosol. *European Journal of Soil Science* **2014**, *65* (5), 684–692. https://doi.org/10.1111/ejss.12157.
(54) Wada, K.; Harward, M. E. Amorphous Clay Constituents of Soils. In *Advances in Agronomy*; Brady, N. C., Ed.; Academic Press, 1974; Vol. 26, pp 211–260. https://doi.org/10.1016/S0065-2113(08)60872-X.
(55) Henmi, T.; Wada, K. Morphology and Composition of Allophane. *American Mineralogist* **1976**, *61* (5–6), 379–390.
(56) Vilgé-Ritter, A.; Rose, J.; Masion, A.; Bottero, J.-Y.; Lainé, J.-M. Chemistry and Structure of Aggregates Formed with Fe-Salts and Natural Organic Matter. *Colloids and Surfaces A: Physicochemical and Engineering Aspects* **1999**, *147* (3), 297–308. https://doi.org/10.1016/S0927-7757(98)00325-2.
(57) Schwertmann, U.; Wagner, F.; Knicker, H. Ferrihydrite–Humic Associations. *Soil Science Society of America Journal* **2005**, *69* (4), 1009–1015. https://doi.org/10.2136/sssaj2004.0274.
(58) Wagai, R.; Mayer, L. M. Sorptive Stabilization of Organic Matter in Soils by Hydrous Iron Oxides. *Geochimica et Cosmochimica Acta* **2007**, *71* (1), 25–35. https://doi.org/10.1016/j.gca.2006.08.047.

(59) Karlsson, T.; Persson, P.; Skyllberg, U.; Mörth, C.-M.; Giesler, R. Characterization of Iron(III) in Organic Soils Using Extended X-Ray Absorption Fine Structure Spectroscopy. *Environ Sci Technol* **2008**, *42* (15), 5449–5454. https://doi.org/10.1021/es800322j.
(60) Lalonde, K.; Mucci, A.; Ouellet, A.; Gélinas, Y. Preservation of Organic Matter in Sediments Promoted by Iron. *Nature* **2012**, *483* (7388), 198–200. https://doi.org/10.1038/nature10855.
(61) Nitzsche, K. N.; Kayler, Z. E.; Premke, K.; Gessler, A.; Wagai, R. Divergent Roles of Iron and Aluminum in Sediment Organic Matter Association at the Terrestrial–Aquatic Interface. *Biogeochemistry* **2022**, *157* (3), 355–378. https://doi.org/10.1007/s10533-021-00878-5.
(62) Filimonova, S.; Kaufhold, S.; Wagner, F. E.; Häusler, W.; Kögel-Knabner, I. The Role of Allophane Nano-Structure and Fe Oxide Speciation for Hosting Soil Organic Matter in an Allophanic Andosol. *Geochimica et Cosmochimica Acta* **2016**, *180*, 284–302. https://doi.org/10.1016/j.gca.2016.02.033.
(63) ThomasArrigo, L. K.; Kretzschmar, R. Iron Speciation Changes and Mobilization of Colloids during Redox Cycling in Fe-Rich, Icelandic Peat Soils. *Geoderma* **2022**, *428*, 116217. https://doi.org/10.1016/j.geoderma.2022.116217.
(64) Scheel, T.; Dörfler, C.; Kalbitz, K. Precipitation of Dissolved Organic Matter by Aluminum Stabilizes Carbon in Acidic Forest Soils. *Soil Science Society of America Journal* **2007**, *71* (1), 64–74. https://doi.org/10.2136/sssaj2006.0111.
(65) Schneider, M. P. W.; Scheel, T.; Mikutta, R.; van Hees, P.; Kaiser, K.; Kalbitz, K. Sorptive Stabilization of Organic Matter by Amorphous Al Hydroxide. *Geochimica et Cosmochimica Acta* **2010**, *74* (5), 1606–1619. https://doi.org/10.1016/j.gca.2009.12.017.
(66) Pokrovski, G. S.; Schott, J. Experimental Study of the Complexation of Silicon and Germanium with Aqueous Organic Species: Implications for Germanium and Silicon Transport and Ge/Si Ratio in Natural Waters. *Geochimica et Cosmochimica Acta* **1998**, *62* (21), 3413–3428. https://doi.org/10.1016/S0016-7037(98)00249-X.
(67) Doelsch, E.; Rose, J.; Masion, A.; Bottero, J. Y.; Nahon, D.; Bertsch, P. M. Speciation and Crystal Chemistry of Iron(III) Chloride Hydrolyzed in the Presence of SiO_4 Ligands. 1. An Fe K-Edge EXAFS Study. *Langmuir* **2000**, *16* (10), 4726–4731. https://doi.org/10.1021/la991378h.
(68) Doelsch, E.; Stone, W. E. E.; Petit, S.; Masion, A.; Rose, J.; Bottero, J.-Y.; Nahon, D. Speciation and Crystal Chemistry of Fe(III) Chloride Hydrolyzed in the Presence of SiO4 Ligands. 2. Characterization of Si−Fe Aggregates by FTIR and 29Si Solid-State NMR. *Langmuir* **2001**, *17* (5), 1399–1405. https://doi.org/10.1021/la0013188.
(69) Châtellier, X.; West, M. M.; Rose, J.; Fortin, D.; Leppard, G. G.; Ferris, F. G. Characterization of Iron-Oxides Formed by Oxidation of Ferrous Ions in the Presence of Various Bacterial Species and Inorganic Ligands. *Geomicrobiology Journal* **2004**, *21* (2), 99–112. https://doi.org/10.1080/01490450490266343.
(70) Lenhardt, K. R.; Breitzke, H.; Buntkowsky, G.; Mikutta, C.; Rennert, T. Interactions of Dissolved Organic Matter with Short-Range Ordered Aluminosilicates by Adsorption and Co-Precipitation. *Geoderma* **2022**, *423*, 115960. https://doi.org/10.1016/j.geoderma.2022.115960.
(71) Jones, A. M.; Collins, R. N.; Rose, J.; Waite, T. D. The Effect of Silica and Natural Organic Matter on the Fe(II)-Catalysed Transformation and Reactivity of Fe(III) Minerals.

Geochimica et Cosmochimica Acta **2009**, *73* (15), 4409–4422. https://doi.org/10.1016/j.gca.2009.04.025.

(72) Keiluweit, M.; Bougoure, J. J.; Nico, P. S.; Pett-Ridge, J.; Weber, P. K.; Kleber, M. Mineral Protection of Soil Carbon Counteracted by Root Exudates. *Nature Climate Change* **2015**, *5* (6), 588–595. https://doi.org/10.1038/nclimate2580.

(73) Jilling, A.; Keiluweit, M.; Gutknecht, J. L. M.; Grandy, A. S. Priming Mechanisms Providing Plants and Microbes Access to Mineral-Associated Organic Matter. *Soil Biology and Biochemistry* **2021**, *158*, 108265. https://doi.org/10.1016/j.soilbio.2021.108265.

(74) Bernard, L.; Basile-Doelsch, I.; Derrien, D.; Fanin, N.; Fontaine, S.; Guenet, B.; Karimi, B.; Marsden, C.; Maron, P.-A. Advancing the Mechanistic Understanding of the Priming Effect on Soil Organic Matter Mineralisation. *Functional Ecology* **2022**, *n/a* (n/a). https://doi.org/10.1111/1365-2435.14038.

(75) Arredondo, M. G.; Fang, Y.; Jones, M.; Yabusaki, S. B.; Cardon, Z.; Keiluweit, M. Resolving Dynamic Mineral-Organic Interactions in the Rhizosphere by Combining In-Situ Microsensors with Plant-Soil Reactive Transport Modeling. Rochester, NY March 24, 2023. https://doi.org/10.2139/ssrn.4385696.

(76) Li, H.; Bölscher, T.; Winnick, M.; Tfaily, M. M.; Cardon, Z. G.; Keiluweit, M. Simple Plant and Microbial Exudates Destabilize Mineral-Associated Organic Matter via Multiple Pathways. *Environ. Sci. Technol.* **2017**, *55* (5), 3389–3398. https://doi.org/10.1021/acs.est.0c04592.

(77) Wagai, R.; Kajiura, M.; Uchida, M.; Asano, M. Distinctive Roles of Two Aggregate Binding Agents in Allophanic Andisols: Young Carbon and Poorly-Crystalline Metal Phases with Old Carbon. *Soil Systems* **2018**, *2* (2), 29. https://doi.org/10.3390/soilsystems2020029.

(78) Wagai, R.; Kajiura, M.; Asano, M. Iron and Aluminum Association with Microbially Processed Organic Matter via Meso-Density Aggregate Formation across Soils: Organo-Metallic Glue Hypothesis. *SOIL* **2020**, *6* (2), 597–627. https://doi.org/10.5194/soil-6-597-2020.